Microstructure-informed prediction of hardening in ion-irradiated reactor pressure vessel steels

Libang Lai, Jann-Erik Brandenburg, Paul Chekhonin, Arnaud Duplessi, Fabien Cuvilly, Auriane Etienne, Bertrand Radiguet, David Rafaja, Frank Bergner

metals

MDPI

Article

Microstructure-Informed Prediction of Hardening in Ion-Irradiated Reactor Pressure Vessel Steels

Libang Lai [1,2,*], Jann-Erik Brandenburg [1], Paul Chekhonin [1], Arnaud Duplessi [3], Fabien Cuvilly [3], Auriane Etienne [3], Bertrand Radiguet [3], David Rafaja [2] and Frank Bergner [1]

[1] Helmholtz-Zentrum Dresden-Rossendorf, Bautzner Landstr. 400, 01328 Dresden, Germany
[2] Institute of Materials Science, Technische Universität Bergakademie Freiberg, Gustav-Zeuner-Str. 5, 09599 Freiberg, Germany
[3] Univ Rouen Normandie, INSA Rouen Normandie, CNRS, Normandie Univ, GPM UMR 6634, F-76000 Rouen, France
* Correspondence: l.lai@hzdr.de

Abstract: Ion irradiation combined with nanoindentation is a promising tool for studying irradiation-induced hardening of nuclear materials, including reactor pressure vessel (RPV) steels. For RPV steels, the major sources of hardening are nm-sized irradiation-induced dislocation loops and solute atom clusters, both representing barriers for dislocation glide. The dispersed barrier hardening (DBH) model provides a link between the irradiation-induced nanofeatures and hardening. However, a number of details of the DBH model still require consideration. These include the role of the unirradiated microstructure, the proper treatment of the indentation size effect (ISE), and the appropriate superposition rule of individual hardening contributions. In the present study, two well-characterized RPV steels, each ion-irradiated up to two different levels of displacement damage, were investigated. Dislocation loops and solute atom clusters were characterized by transmission electron microscopy and atom probe tomography, respectively. Nanoindentation with a Berkovich indenter was used to measure indentation hardness as a function of the contact depth. In the present paper, the measured hardening profiles are compared with predictions based on different DBH models. Conclusions about the appropriate superposition rule and the consideration of the ISE (in terms of geometrically necessary dislocations) are drawn.

Keywords: reactor pressure vessel steels; ion irradiation; microstructure characterization; transmission electron microscopy; atom probe tomography; nanoindentation; hardening

Citation: Lai, L.; Brandenburg, J.-E.; Chekhonin, P.; Duplessi, A.; Cuvilly, F.; Etienne, A.; Radiguet, B.; Rafaja, D.; Bergner, F. Microstructure-Informed Prediction of Hardening in Ion-Irradiated Reactor Pressure Vessel Steels. *Metals* **2024**, *14*, 257. https://doi.org/10.3390/met14030257

Academic Editor: Hannu Hänninen

Received: 29 January 2024
Revised: 18 February 2024
Accepted: 19 February 2024
Published: 21 February 2024

1. Introduction

Ion irradiation is a popular and promising tool to emulate neutron irradiation effects on the irradiation-induced formation of defects and hardening of reactor pressure vessels (RPV) steels [1–8]. Ion irradiation can be performed quickly with both an easy control of different variables and little or no residual radioactivity. However, the scattering cross-section of accelerated ions differs strongly from the scattering cross-section of thermal neutrons, which results in different penetration depths and irradiation damage when using the respective technique. While the penetration depth of neutrons is on the order of magnitude of 1 m, the penetration depth of accelerated ions is a few micrometers. Therefore, the normal Vickers hardness test cannot be applied to ion-irradiated samples. Nanoindentation is a viable technique to measure the hardness of the samples at small depths. However, using nanoindentation, there are also issues accompanying the measurement of the hardness on ion-irradiated samples, such as the indentation size effect (ISE) [9–12] and the plastic zone reaching into the unirradiated substrate [10].

The combination of ion irradiation and nanoindentation, as attractive as it may be for accelerated studies of the irradiation behavior of materials, introduces several challenges, including mutual interactions of pre-existing, irradiation-induced, and indentation-induced

defects. A literature review indicates two major objectives of related studies. The first is the derivation of a bulk-equivalent hardness for the best possible transferability towards the neutron irradiation [13,14]. The second is the description and understanding of the hardness profile of ion-irradiated layers [15–19], irrespective of ion-neutron transferability (obviously, such understanding can also contribute to the solution of transferability issues). The second type of objective is pursued in the present study, which is dedicated to the microstructure and hardening of ion-irradiated RPV steels. The key constituent is the microstructure-informed prediction of hardening and the comparison of the predicted hardness profile with the measured nanoindentation response.

Microstructure-informed predictions of hardening have been reported by several groups [20–27], most of them referring to the dispersed-barrier hardening (DBH) model [20,21,23]. Chen et al. [21] characterized the irradiation-induced dislocation loops as a function of the distance from the surface of ion-irradiated stainless steel samples. These authors compared the predicted hardening averaged over the hemispherical plastic zone with the hardening measured for a certain indentation depth. This corresponds to a linear superposition of the hardening contributions arising from pre-existing and irradiation-induced defects. The same type of superposition was considered by Kareer et al. [15] for Fe-Cr alloys and by Röder et al. [16] for RPV steels. Vogel et al. [17] applied a microstructure-informed DBH model to Fe-9Cr and ODS-Fe-9Cr and compared linear and square superposition of pre-existing and irradiation-induced hardening contributions. For square superposition, the ISE was considered in terms of geometrically necessary dislocations (GNDs). However, linear superposition with the effect of GNDs in the unirradiated and irradiated conditions canceling each other appeared to work best. This motivated the application of the respective model version in the present study.

Using simulations of the dislocation-obstacle interaction, Foreman and Makin [28] found out that the superposition of hardening contributions arising from two families of obstacles depends on both relative strengths and the number densities of the families of obstacles. For obstacles of similar strength, square superposition was reported to work well. In contrast, a small fraction of strong obstacles added to a family of weak obstacles gives rise to much more hardening than predicted by square superposition. Even more relevant for the present context, Xiao et al. [18] compared linear and square superposition of the hardening contributions arising from pre-existing and ion-irradiation-induced defects and concluded that linear and square superposition perform equally well in a certain range of the indentation depth, while square superposition is favorable at larger depths. Most recently, Zhu et al. [29] introduced a model with mixed superposition based on the distinction of weak and strong obstacles and the application of the square superposition for both weak with weak and strong with strong obstacles and linear superposition for weak with strong obstacles.

Monnet [30] reviewed the hardening mechanisms, the resulting analytic expressions, and their superposition relevant to nuclear materials, including irradiated RPV steels. Monnet focused on extensions of the original DBH model, taking into account the results of sophisticated dislocation simulations. Comparisons of the hardening predicted for neutron-irradiated RPV steels and Fe-Cr alloys with reported experimental results indicated good agreement and justified adoption in the present study. However, Monnet's work has not yet been applied to the special case of ion irradiation in combination with nanoindentation. Therefore, the presence of both GNDs and damage profiles has to be added to this framework.

Mattucci et al. [31] reported a microstructure-informed prediction of hardening in proton-irradiated Ni and subtracted it from the measured depth-dependent indentation hardness. At depths of 700 nm and below, the difference was found to be significantly larger than the hardness of the unirradiated reference, indicating the important role of GNDs. These authors' explanation is based on the assumption (and arguments in favor) of a larger density of GNDs in the irradiated compared with the unirradiated material.

The present paper establishes a model for the prediction of the ion-irradiation-induced hardening of RPV steels based on the reported ideas. Results of nanoindentation tests are reported, including modulus-based pile-up corrections. A previous study based on scanning electron microscopy (SEM) and transmission electron microscopy (TEM) [32] investigated the pre-existing microstructures, the irradiation-induced dislocation loops for the same materials and irradiation conditions. The current study briefly summarizes these published results, which are important for microstructure-informed predictions. These results are complemented by the distribution of irradiation-induced solute atom clusters obtained using atom probe tomography (APT) and the results of the nanoindentation testing. Finally, the hardening concluded from the results of the nanoindentation is compared with the hardening predicted using the microstructure-informed models.

2. Materials and Methods

2.1. Materials and Samples Preparation

Two commercial RPV steels with body-centered cubic (bcc) structure, here referred to as ANP-6 and ANP-10, are investigated in this study. Both of them were provided by Framatome GmbH (Erlangen, Germany) as broken Charpy-V specimens. ANP-6 is a western second-generation RPV weld of type S3NiMo/OP41TT, while ANP-10 is a western 2nd/3rd generation RPV steel (forging) of type 22NiMoCr3-7. The chemical compositions of the steels, analyzed by means of optical emission spectroscopy, are given in Table 1 [33].

Table 1. Chemical compositions in wt. % (Fe as balance).

Material	C	Mn	Si	Cr	Ni	Mo	V	P	Cu
ANP-6	0.05	1.41	0.15	0.07	1.69	0.46	0.004	0.012	0.08
ANP-10	0.18	0.81	0.15	0.40	0.96	0.53	<0.01	0.006	0.09

Larger blocks of the as-received materials in an unirradiated state were cut into small rectangular samples by electrical discharge machining. Mechanical sample preparation was performed before ion irradiation with the following steps:

- Grinding with SiC-paper down to 2500 grid,
- Mechanical polishing with 3 µm and 1 µm diamond paste,
- Fine polishing with 60 nm silica suspension (Mastermet, Buehler, Leinfelden-Echterdingen, Germany).

Initial trials included electro-polishing as a final preparation step, but undesirable surface damage was observed in the resulting sample surface. Comparison between electro-polished and mechanically fine-polished samples indicated no significant difference in the measured nanohardness. It was, therefore, decided to omit the electro-polishing step after mechanical fine polishing for all subsequently prepared samples. Comprehensive analyses of the microstructures and the resulting hardening mechanisms of the unirradiated materials were reported in [32].

2.2. Ion Irradiation

The ion irradiation was performed in the Ion Beam Center at Helmholtz–Zentrum Dresden–Rossendorf. The samples were irradiated at 300 °C with Fe^{2+} ions having an energy of 5 MeV. The irradiation conditions for both materials are summarized in Table 2.

Table 2. Summary of Fe^{2+} irradiation conditions.

Ion Energy (MeV)	Flux (cm^{-2}/s)	Fluence (cm^{-2})	Irradiation Time (h)	Temperature (°C)	Dose at Depth of 0.5 µm (dpa)
5	1.25×10^{11}	2.67×10^{14}	0.6	300	0.1
5	1.25×10^{11}	2.67×10^{15}	6	300	1

The damage and implantation depth profiles were calculated using the software Stopping and Range of Ions in Matter (SRIM) 2013 [34] with the quick Kinchin–Pease approximation and a displacement threshold energy of 40 eV [35]. The widely accepted unit of displacement damage is "displacement per atom" (dpa), which was introduced in [36,37]. The profiles of displacement damage in units of dpa and injected interstitials in units of atomic parts per million (appm) are shown in Figure 1. The two different doses of 0.1 and 1 dpa were reached at a depth of 500 nm.

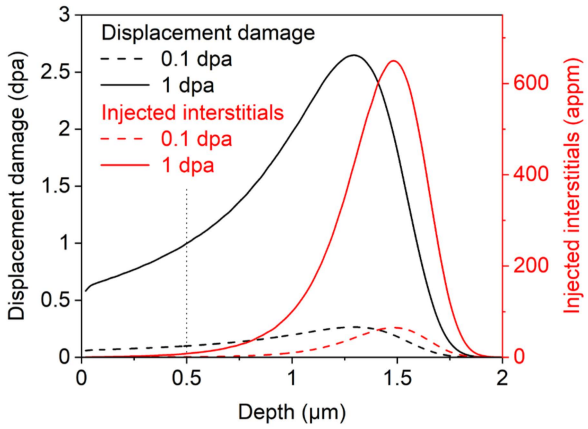

Figure 1. Depth profile of displacement damage and injected interstitials for 0.1 dpa (dashed lines) and 1 dpa (solid lines) calculated by SRIM.

2.3. Transmission Electron Microscopy (TEM)

After irradiation, cross-sectional samples were lifted out as lamella in a wedge shape with around 10 µm width, a depth of at least 3 µm, and a thickness between 60 and 200 nm at the relevant areas by the technique of focused ion beam (FIB). On the cross-sectional samples, a Talos 200 FEG TEM (FEI, Eindhoven, The Netherlands) was applied to image dislocation loops and to measure their size and number density. Scanning transmission electron microscope (STEM) mode was used during imaging. More details on the STEM experiments and analysis were reported in [32].

2.4. Atom Probe Tomography (APT)

Ion-irradiated ANP-6 and ANP-10 steels were received as square plates having a size of 1×1 cm^2. The samples for APT analysis were prepared as thin needles with an end radius smaller than 50 nm using lift-out and annular milling methods. The long axis direction of the needles is parallel to the sample surface normal. ANP-6 samples were prepared in a Zeiss XB 540 SEM-FIB (Carl Zeiss, Oberkochen, Germany) using 30 keV Ga ions. The final step (cleaning step) was performed using 2 keV Ga ions to remove the damaged and implanted layer. ANP-10 samples were prepared in a Thermo Fisher plasma-FIB Helios SEM-FIB (Thermo Fisher, Eindhoven, The Netherlands) using 30 keV Xe ions. The cleaning step was performed with Xe ions under 12 kV accelerating voltage. Since the damage profile is not homogeneous through the irradiated depth from the sample surface, the APT samples were prepared in order to attain the tip apex at depth ranges of 400–500, 800–900, and 1150–1250 nm. This allows for the description of the microstructure at different depths. To ensure the representativeness of the results, at least two different chunks and two different needles per chunk were analyzed for each condition.

The APT investigations were carried out using a Cameca LEAP 4000 XHR and a Cameca LEAP 5000 XR (Ametek-Cameca, Madison, WI, USA). Standard analysis conditions for RPV steels were used: Voltage mode, a pulse fraction equal to 20% of the standing voltage, a pulse repetition rate equal to 200 kHz, and a specimen temperature between 50 and 60 K.

The analyzed volumes were reconstructed using the commercial IVAS 3.8.16 software. All volumes were reconstructed using the voltage curve to estimate radius evolution and adjusting compression factor and field factor in order to attain good angles between crystallographic poles and good interplanar distances. Further data treatment was performed using the Gpm 3d-SAT software version 7 (IDDN.FR.001.430017.000.S.P.2020.000.10000). The cluster analysis was performed using the isoposition method [38]. The APT results presented here for each condition are average values from 3 to 5 datasets obtained from 2 different chunks in order to ensure the reproducibility of the results. It represents volume from 1.5 to 3 $\times$ 10^5 nm^3 for each condition. The only exception is the ANP6 irradiated at 1 dpa and analyzed at 1200 nm depth, for which only 3 $\times$ 10^4 nm^3 was analyzed yet.

2.5. Nanoindentation

The indentation hardness of all samples was measured on the sample surface using an ASMEC UNAT nanoindenter. In order to obtain a depth profile of the indentation hardness, the quasi-continuous stiffness measurement (QCSM) method was applied. All hardness measurements were performed with the same Berkovich-geometry indenter tip. The contact area function of the tip and the device compliance were calibrated at the same time using an automated method included in the UNAT device software InspectorX version 5.3.4. The method is based on measuring the elastic modulus of two different standard samples (here, fused quartz and sapphire) and varying the calibration functions for contact area and device compliance until the correct elastic modulus for both materials is obtained.

After finding the correct position of the sample surface, the load was increased to 50 mN over 250 s and kept constant for 20 s to monitor potential creep. The load increase was interrupted with (75) intervals to superimpose, for each interval, a sinusoidal vibration for 3 s (frequency: 8.494 Hz, amplitude: 0.3 V) and quasi-continuously measure the contact stiffness S according to the QCSM method. Afterward, the sample was partially unloaded to 5 mN, and the load was kept constant again for drift correction before final unloading. During all segments, the nanoindenter was operated in load-controlled mode. Multiple hardness measurements were conducted for each sample and in a single run. Typically, 39 indentations and 3 approach points were performed in a 6 $\times$ 7 array with a distance of 40 µm between the points.

The load-indentation depth (F-h) curves were acquired after certain fitting and drift corrections. Then, the indentation hardness H_{IT} and the reduced elastic modulus E_r at each load F corresponding to a hold interval of the QCSM method were calculated according to [11,39–41]:

$$H_{IT} = \frac{F}{A_p(h_c)} \tag{1}$$

$$h_c = h - \epsilon\frac{F}{S} \tag{2}$$

$$E_r = \frac{\sqrt{\pi}S}{2\sqrt{A_p(h_c)}} \tag{3}$$

In these equations, $A_p(h_c)$ is the calibrated area function (projected area) and h_c is the contact depth, which differs from the measured indentation depth h due to the elastic deformation of the sample surface. ϵ = 0.75 is the geometry factor for a Berkovich indenter. S is the contact stiffness acquired by the QCSM method. The indentation modulus E_{IT} is related to the reduced modulus as follows:

$$\frac{1}{E_r} = \frac{(1-\nu^2)}{E_{IT}} + \frac{(1-\nu_i^2)}{E_i} \tag{4}$$

where $\nu = 0.29$ is the Poisson's ratio of the steel; $\nu_i = 0.07$ and $E_i = 1141$ GPa are Poisson's ratio and Young's modulus of the indenter, respectively. Based on Equations (1)–(4), H_{IT}

and E_{IT} (together with their statistical errors) are obtained as functions of the contact depth h_c.

An important issue for nanoindentation is the well-known pile-up effect [42,43], which can cause systematic errors in both the indentation modulus and hardness. There are two methods to correct the error caused by the pile-up effect. The first one is based on atom force microscopy to measure the 'actual' contact area [42,43]. The second one, applied below, uses the measured indentation modulus [11,44].

Let $A_{p,a}$ be the actual projected contact area with the pile-up effect taken into account. Equations (1) and (3) then indicate the following equality of the ratios of corrected and as-measured indentation hardness and reduced modulus [11,44]:

$$\frac{H_{IT,corr}}{H_{IT}} = \left(\frac{E_{r,corr}}{E_r}\right)^2 = \frac{A_p}{A_{p,a}} \quad (5)$$

The left-hand part of Equation (5) is the basis for the modulus-based pile-up correction. Young's modulus for ANP-6 and ANP-10 is known to be close to $E = 210$ GPa independent of the irradiation condition applied. The corresponding value of $E_r = 191$ GPa resulting from Equation (4) has been substituted for $E_{r,corr}$ in Equation (5) in order to calculate the corrected indentation hardness $H_{IT,corr}$.

3. Results

3.1. Unirradiated Microstructure

The unirradiated microstructures were characterized comprehensively and reported in a previous work [32]. Table 3 summarizes the necessary unirradiated microstructure parameters that will be used to establish the model in Section 4.

Table 3. Unirradiated microstructure parameters [32].

Properties	ANP-6	ANP-10
Grain size (μm)	2.9	5.5
Dislocation density (m^{-2})	3.2×10^{14}	5.2×10^{13}
Mean size of carbides (nm)	65	67
Number density of carbides (m^{-3})	8.6×10^{19}	2.9×10^{20}

3.2. Irradiated Microstructure

3.2.1. Depth Profile of Dislocation Loops

The results of the STEM experiments, in particular the number density (number per volume) and size (mean diameter) of irradiation-induced loops as a function of their distance from the surface of cross-sectional samples, were reported in detail and compared with the damage profiles (Figure 1) in our previous work [32]. The reported results are summarized in Figure 2 for the materials and irradiation conditions of interest. Errors for number density and the size of loops are approximately 10% and 20%, respectively, which was reported in detail in [32].

3.2.2. Depth Profile of Solute Atom Clusters

APT revealed complex microstructures at different depths, with segregation of solute atoms along the dislocation lines and dislocation loops and the formation of solute clusters inside the matrix and along dislocations. These details will be the topic of another publication.

Since the population of dislocation loops was already quantified by TEM, APT data were used mainly to quantify the size and number density of the clusters of solute atoms, which are required as input parameters for the hardening model. The APT analysis demonstrated that the clusters are enriched with Mn, Ni, and Si, Ni being dominant. The cluster composition does not exhibit a significant difference between the two materials as a function of depth. It is important to note that the number density of clusters in the vicinity of sinks, such as dislocation lines or loops, is not the most pertinent parameter for

hardening estimation since it depends on the number of sinks intercepted in the analyzed APT volumes. Thus, quantitative results were considered only for clusters dispersed in the matrix. This choice is supported by the experimental finding: clusters in the matrix are dominant over clusters at sinks in terms of number density. The results at depth ranges of 400–500, 800–900, and 1150–1250 nm are reported in Tables 4 and 5 for ANP-6 and ANP-10, respectively.

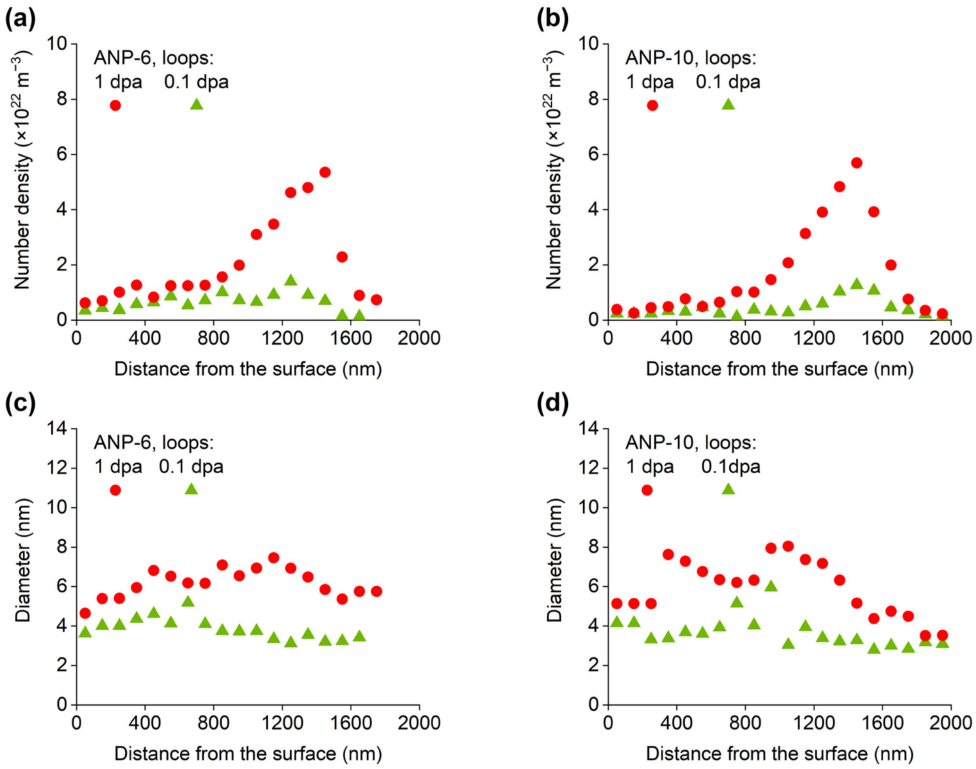

Figure 2. Depth profiles of loops number densities in (**a**) ANP-6, (**b**) ANP-10, and mean diameters in (**c**) ANP-6, (**d**) ANP-10.

Table 4. Measured sizes and number densities of clusters in the matrix for ANP-6.

ANP-6		**0.1 dpa**			**1 dpa**	
Depth (nm)	400–500	800–900	1150–1250	400–500	800–900	1150–1250
Size (nm)	2.9	2.7	2.8	4.0	3.5	4.4
Number Density ($\times 10^{22}$ m^{-3})	7.2	10.4	9.8	16.1	28	31

Table 5. Measured sizes and number densities of clusters in the matrix for ANP-10. The sample irradiated at 0.1 dpa has not yet been analyzed by APT in a depth range of 1150–1250 nm.

ANP-10		**0.1 dpa**			**1 dpa**	
Depth (nm)	400–500	800–900	1150–1250	400–500	800–900	1150–1250
Size (nm)	3	2.7	-	3.1	3.7	3
Number Density ($\times 10^{22}$ m^{-3})	2.2	2.55	-	16	27.4	41

For both ANP-6 and ANP-10, irradiation at 1 dpa results in a higher density of slightly larger solute atom clusters than at irradiation at 0.1 dpa. There is no significant difference in the cluster size between the two materials at the same irradiation level. In samples irradiated at 1 dpa, both materials exhibit a similar number density of clusters, while in

samples irradiated at 0.1 dpa, ANP-6 shows a higher number density in comparison to ANP-10. The effect of irradiation conditions and material composition on microstructural evolution is out of the scope of this paper and will be discussed in another article.

For the microstructure model to be established, information about the depth dependence of the cluster size and number density is required. As shown in Figure 3, four segments are separated for the data distribution of clusters from the irradiated surface to the unirradiated substrate. The first segment extends from 0 to 700 nm; data measured at a depth range of 400–500 nm are distributed uniformly in this segment. The second segment ranges from 700 to 1000 nm; data measured at a depth range of 800–900 nm are taken as representative of this segment. The third segment covers the range from 1000 nm to the peak position of the number density of loops measured previously (from 1350 to 1550 nm); data measured at a depth range of 1150–1250 nm are distributed uniformly in this segment. The last segment goes beyond the 'peak position', i.e., to the unirradiated substrate. In this last segment, the number density of clusters is assumed to decrease linearly to 0 from the previous segment, while the size remains unchanged. This is justified since the size of clusters does not show a significant difference as a function of the distance from the surface, while the number density depends on the displacement damage (see Figure 1). Errors for number density and size of clusters are approximately 10% and 20%, respectively. The number density and size distribution of clusters were determined using the Gpm 3d-SAT software version 7, as mentioned in Section 2.4. The error of the number density was derived from the square root of the total number of clusters (statistical error) within the whole analyzed volume for each condition. The error of the average size was derived from the size distribution of the clusters (standard deviation).

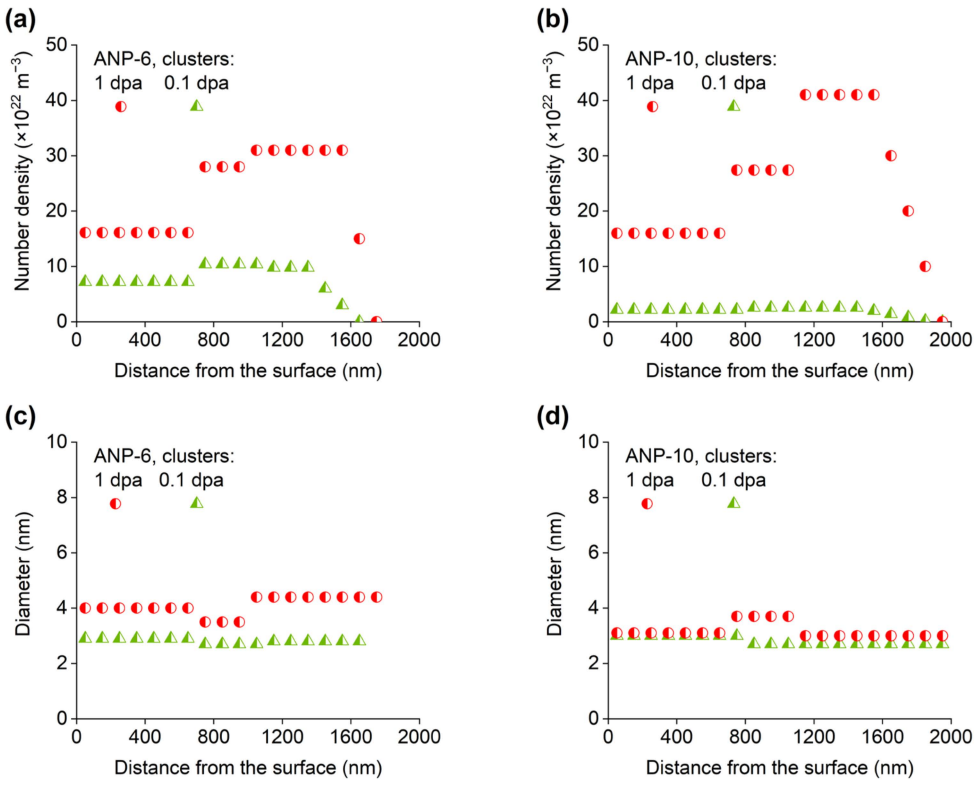

Figure 3. Depth profiles of clusters number densities for (**a**) ANP-6, (**b**) ANP-10, and mean diameters for (**c**) ANP-6, (**d**) ANP-10.

3.3. Nanoindentation

The original indentation hardness H_{IT} measured in the respective materials (ANP-6 and ANP-10) as a function of the contact depth h_c is plotted in Figure 4. Black, green, and red curves represent unirradiated, irradiated with 0.1 dpa, and irradiated with 1 dpa

samples, respectively. For the unirradiated condition, the indentation hardness should decrease with increasing contact depth because of the ISE, as it is observed for depths larger than 100 nm. The apparent softening at smaller depths may be due to experimental issues, and this range will be ignored below.

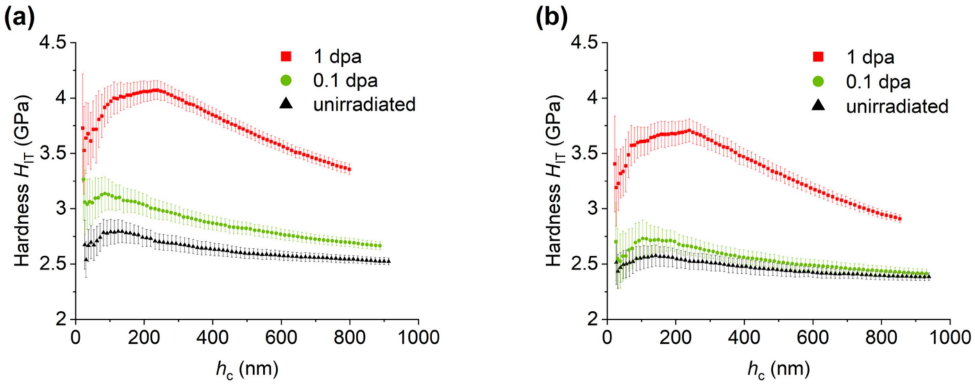

Figure 4. Measured H_{IT} as a function of h_c for (**a**) ANP-6 and (**b**) ANP-10.

The increase in the hardness due to the ion irradiation (0.1 dpa and 1 dpa), ΔH_{IT}, as a function of $h_{c,}$ is shown in Figure 5. The hardening exhibits a maximum at the contact depth of approximately 250 to 300 nm. At higher depths, the hardness difference decreases mainly due to the substrate effect. At smaller contact depths, the hardness difference decreases because the displacement damage, as well as the related concentrations of clusters and loops, decrease towards the surface.

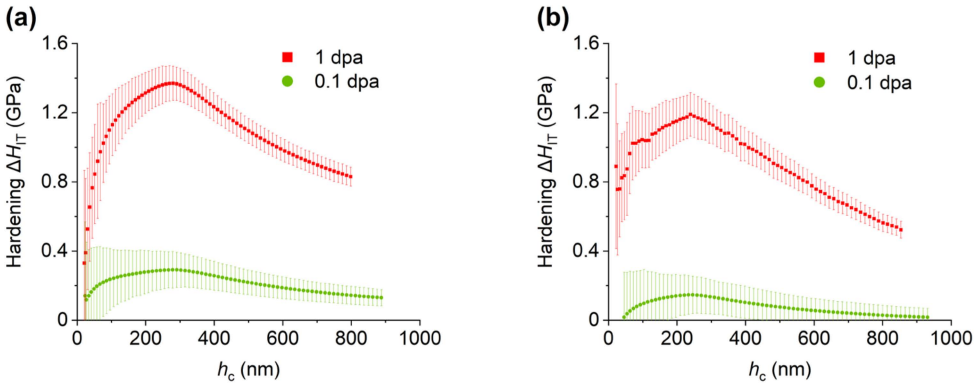

Figure 5. Measured ΔH_{IT} as a function of h_c for (**a**) ANP-6 and (**b**) ANP-10.

For both materials and all irradiation conditions, the indentation modulus E_{IT} is plotted in Figure 6 as a function of contact depth h_c. It was found that the indentation moduli for the 0.1 dpa and 1 dpa irradiations are close to each other and only slightly higher than for the respective unirradiated reference material (by less than 5%). Therefore, the indentation moduli measured in unirradiated samples, and samples irradiated by 0.1 dpa and 1 dpa were treated together. The resulting empirical fit curves according to Equations (6) and (7) are included in the plots for ANP-6 and ANP-10, respectively (see Figure 6).

$$E_{IT} = 219.4 + 52.5e^{\left(\frac{-h_c}{225.7}\right)} \quad (6)$$

$$E_{IT} = 232.8 + 66.3e^{\left(\frac{-h_c}{210.5}\right)} \quad (7)$$

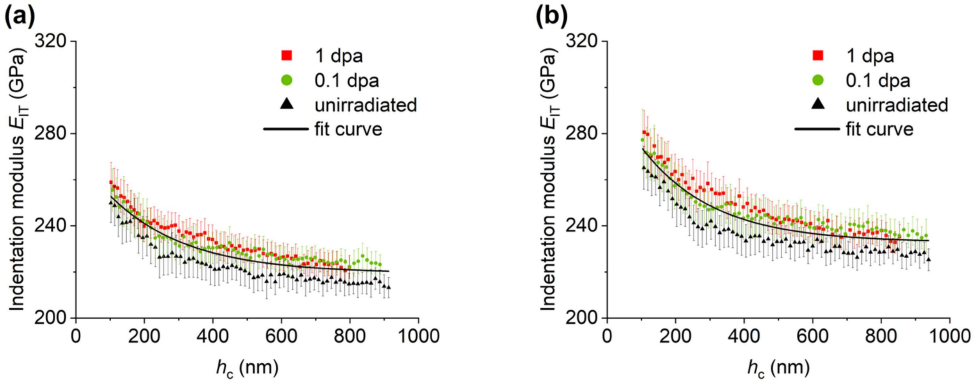

Figure 6. Indentation modulus E_{IT} as a function of h_c for (**a**) ANP-6 and (**b**) ANP-10. The fits are described by Equations (6) and (7), respectively.

Equations (6) and (7) were used to calculate the reduced modulus E_r according to Equation (4) and the pile-up correction factor $(E_{r,corr}/E_r)^2$ according to Equation (5). Thus, the corrected hardness $H_{IT,corr}$ is derived as a function of the contact depth h_c. Plots of as-measured and corrected ΔH_{IT} as functions of h_c are displayed in Figure 7a,b for ANP-6 and ANP-10, respectively. Data points below 100 nm contact depth have been omitted because of diverging experimental errors. The correction results in a decrease in the hardening in the whole range of contact depths. It is worth noting that in the case of 1 dpa, the peak positions of the as-measured and corrected curves approximately coincide. The corrected hardening $\Delta H_{IT,corr}$ will be used for the comparison of the models in the next section. For convenience, the subscript 'IT,corr' will be omitted.

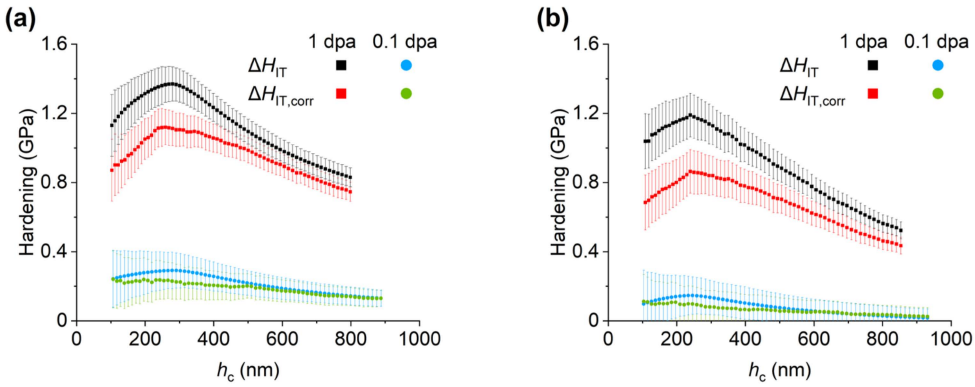

Figure 7. Corrected hardening $\Delta H_{IT,corr,}$ and original ΔH_{IT} as functions of h_c in (**a**) ANP-6 and (**b**) ANP-10.

4. Model

4.1. Theoretical Background

In the present study, the original and extended versions of the DBH model are applied to predict the ion-induced hardening of RPV steels. The general idea for the original DBH model for a single type of barrier [1] (e.g., clusters or loops) is that the hardness increase is controlled mainly by the local lattice strain/stress produced by the dispersed barriers (obstacles):

$$\Delta H = \beta\sigma = \alpha\beta MGb\sqrt{Nd} \quad (8)$$

In Equation (8), ΔH is the hardening and σ the lattice stress. β is a conversion factor for stress to hardness. The value estimation of β will be discussed below. For dislocations, the stress is calculated from the lattice strain, which involves the number density (N), mean diameter (d), and strength (α) of the obstacles, the magnitude of the Burgers vector of the glide dislocations which are pinned by the obstacles (b), the shear modulus of the material

(G) and the Taylor factor (M). N and d are taken from the microstructure characterization (Figures 2 and 3). α depends on the kind of obstacles and varies for different model versions. The specific values will be introduced below. b is 0.248 nm for bcc 1/2 <111>-type line dislocations, assuming all are 1/2 <111>-type. G is 83 GPa [30,45]. M is recommended to be 3.06 [46].

To describe the dependence of the hardening on the depth below the sample surface, we assume a volume fraction model [10]. This means that a weighted average of the indentation hardness is taken with the weights corresponding to the volume fraction covered by a certain depth layer in the indentation plastic zone. The plastic zone is assumed to be approximately hemispherical with a radius proportional to the contact depth, $R = ch_c$. c is a size factor. Therefore, the c parameter affects the effective depth in the material at which the indentation hardness is measured. $c = 7$ was used as a starting point [19,47].

It is important to note that predictions of the values of c and β are available on the basis of the expanding cavity model [48,49]. For linear–elastic ideally plastic materials, the size factor c takes the form [48]:

$$c = \frac{R}{h_c} = \left[\frac{\frac{E}{\sigma_y} \tan\theta + 4(1-2\nu)}{6(1-\nu)\tan^3\theta} \right]^{1/3} \quad (9)$$

The conversion factor is [48]:

$$\beta = \frac{H}{\sigma_y} = \frac{2}{3}\left\{ 1 + \ln\left[\frac{\frac{E}{\sigma_y} \tan\theta + 4(1-2\nu)}{6(1-\nu)} \right] \right\} \quad (10)$$

In Equations (9) and (10), $E = 210$ GPa, $\nu = 0.29$ and σ_y are Young's modulus, Poisson's ratio, and yield stress of the steels, respectively, and $\tan\theta = 0.358$ for a Berkovich tip. The yield stress and the values predicted from the expanding cavity model are summarized in Table 6. The estimates of c are in reasonable agreement with our starting value of $c = 7$. For the value of β, Gao et al. [49] suggested a modification of Equation (10) applicable to power-law hardening materials, $\sigma_t = k\varepsilon_t^n$ with σ_t, ε_t, k and n denoting true stress, true strain, a constant factor and the power-law exponent, respectively.

$$\beta = \frac{H}{\sigma_y} = \frac{2}{3}\left[\left(1 - \frac{1}{n}\right) + \left(\frac{3}{4} + \frac{1}{n}\right)\left(\frac{1}{3}\frac{E}{\sigma_y} cot\theta\right)^n \right] \quad (11)$$

Table 6. Values of measured σ_y, and predicted c and β using Equations (9)–(11).

Material	σ_y (MPa) [33]	c	β (Equation (10))	β (Equation (11))
ANP-6	555	8.9	3.0	4.5
ANP-10	422	9.7	3.2	(4.5) *

* Assumed to be the same as for ANP-6.

The value of the exponent n is equal to the uniform elongation, which is known to be 0.1 (10%) for ANP-6 [50]. The β values calculated according to Equation (11) for ANP-6 are given in Table 6. They will be used in the models applied for ANP-6 and ANP-10.

It is widely accepted that the pre-existing microstructure features (such as grain boundaries, particles, forest dislocations, etc.) do not change during irradiation at levels of displacement damage similar to those in the present study. In the following, four different versions of the DBH model, Case 1 to Case 4, will be discussed. They are briefly motivated here and explained in more detail in Sections 4.2–4.5. In Case 1, the hardness of irradiated materials is assumed to result from the linear superposition of the pre-existing microstructures with irradiation-induced defects. Thus, the hardness of the pre-existing microstructures drops out in the difference between the hardness of irradiated and unirradi-

ated materials. Although pure linear superposition was reported to be inappropriate in the literature [18,28,30], the present study started from this assumption as a baseline because some authors [17,51] reported good agreement for linear superposition. Case 2 considers the hardness of irradiated materials resulting from a mixed (linear and square) superposition of the pre-existing microstructures with irradiation-induced defects, according to Monnet [30]. Moreover, improved expressions for the individual hardness contributions were introduced in the same study. Cases 1 and 2 do not consider the effect of nanoindentation-induced GNDs on hardening, meaning that GNDs are assumed to contribute according to linear superposition (Case 1) or are neglected (Case 2). Cases 3 and 4 are the models developed from Case 2 with additional consideration of GNDs. The hardness contribution due to GNDs is assumed to contribute according to square superposition. Thus, the effect of GNDs on hardening will not drop out. In Case 3, the densities of GNDs induced by the process of nanoindentation are considered equal for the unirradiated and irradiated samples tested at the same contact depth. It is interesting to note that equal densities of GNDs and square superposition were also considered in [17]. In Case 4, these densities are assumed to be different, as proposed by Mattucci et al. [31].

4.2. Case 1

In the model of Vogel et al. [17] applied to Fe-9Cr, the hardening of the irradiated material is calculated as a linear difference between the hardness of the irradiated and unirradiated materials. The hardness of an irradiated material (subscript '*irrad*') was obtained as a linear superposition of the hardness contributions due to the pre-existing microstructure (subscript '*ref*') and irradiation-induced dislocation defects (only loops). Thus, the hardness of the pre-existing microstructure drops out, and the irradiation-induced hardening ΔH accounts only for irradiation-induced loops [17]. For RPV steels, as in the present study, two types of irradiation-induced defects were observed, namely loops (subscript '*l*') and clusters (subscript '*c*'). The hardening contributions arising from loops and clusters are assumed to be added quadratically [30]:

$$\Delta H(h) = H_{irrad} - H_{ref} = \beta\sqrt{\sigma_l^2 + \sigma_c^2} = \frac{\beta MGb}{V_{pz}(h)} \int \sqrt{\alpha_l^2 N_l(z) d_l(z) + \alpha_c^2 N_c(z) d_c(z)} dV \quad (12)$$

where the obstacle strengths of loops and clusters were suggested to be $\alpha_l = 0.333$ [28] and $\alpha_c = 0.1$ [52], respectively. For convenience, the symbol h denotes the contact depth in Equation (12), instead of h_c used in the previous sections. This nomenclature will be applied in all equations below. The results of Case 1 are plotted in Figure 8a,b for ANP-6 and ANP-10, respectively. For ANP-6, the model slightly overestimates the measured hardness increase (after pile-up correction) for the 1 dpa sample below a contact depth of 450 nm and exhibits an underestimation above 450 nm. For the 0.1 dpa sample, the prediction is always overestimated and approximately three times larger than the measured hardening at maximum. The peak position is matched between the model and measured hardening with an initially estimated size factor c = 7 for the plastic zone. For ANP-10, the model with c = 7 gives rise to a deviation of the peak position between the model and measurement. Figure 8b shows that changes in the size factor c for the case of 1 dpa (c = 7, 8, or 9) result in a horizontal shift but not in changes in the height of the curve. This is expected because a larger plastic zone means that the effect of the layer of maximum irradiation damage is encountered at lower contact depths. c = 8 shows the best match of the peak position with the measurement. Therefore, the size factor c is adjusted as 8 for material ANP-10 for all model versions applied, while it remains the same (c = 7) for ANP-6. With c = 8, the microstructure-informed predictions for ANP-10 overestimate the hardening for both 0.1 and 1 dpa.

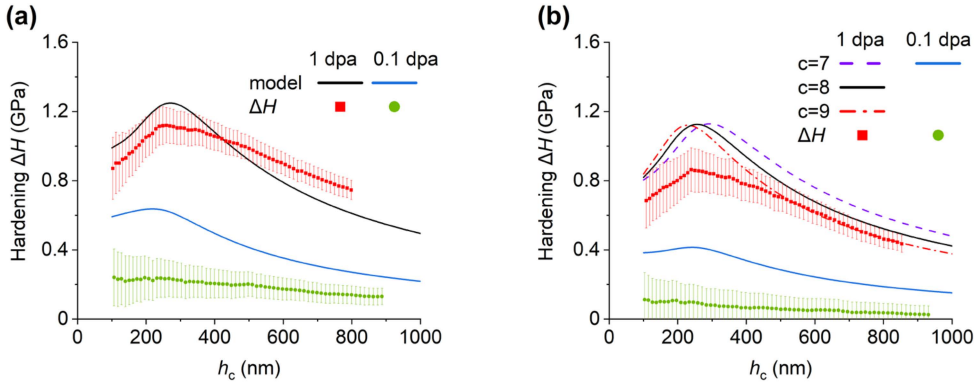

Figure 8. Case 1 model predictions compared with experiments for (**a**) ANP-6 and (**b**) ANP-10. The hardening was calculated as a difference between the hardness of irradiated and unirradiated materials $\Delta H = H_{irrad} - H_{ref}$.

It is worth noting that the empirical size factors inferred from the measured peak position of ΔH agree reasonably well with the predicted size factors (Table 6). In particular, the larger empirical c value observed for ANP-10 compared with ANP-6 is confirmed by the prediction.

4.3. Case 2

In Case 2, the hardening of the irradiated material is calculated as a linear difference between the hardness of the irradiated and unirradiated materials as well. However, unlike Case 1, in Case 2, the hardness of irradiated materials is affected by the pre-existing microstructures and irradiation-induced defects [30]. Thus, it is necessary to explicitly express the hardness contributions of pre-existing microstructures (*ref*). They include solute atoms, grain boundaries, forest dislocations, and particles. The contributions of forest dislocations (d) and particles (p) to the hardness have to be added quadratically [53], while the contributions of solid solution (ss) hardening [30,54,55] and grain boundary (gb) hardening [30] have to be added linearly:

$$H_{ref} = \beta\left(\sqrt{\sigma_d^2 + \sigma_p^2} + \sigma_{ss} + \sigma_{gb}\right) \tag{13}$$

The hardness of the irradiated samples is affected by the same microstructure features in the pre-existing microstructure and, in addition, by the dislocation loops (l) and clusters (c) [30]:

$$H_{irrad} = \beta\left(\sqrt{\sigma_d^2 + \sigma_p^2 + \sigma_l^2 + \sigma_c^2} + \sigma_{ss} + \sigma_{gb}\right) \tag{14}$$

Due to the 'linear behavior,' the contributions of the solid solution and grain boundary hardening do not affect the hardening:

$$\Delta H(h) = H_{irrad} - H_{ref} = \beta\left(\sqrt{\sigma_d^2 + \sigma_p^2 + \sigma_l^2 + \sigma_c^2} - \sqrt{\sigma_d^2 + \sigma_p^2}\right), \tag{15}$$

assuming that the concentration of the alloying atoms and the grain size do not change after the ion irradiation. Because of the quadratic addition of the individual contributions, resulting ΔH is not affected by weak or negligible effects.

The lattice stress induced by the forest dislocations is proportional to the dislocation density ρ_d (see Table 3):

$$\sigma_d = \alpha_d M G b \sqrt{\rho_d} \tag{16}$$

The lattice stress induced by the particles (carbides) is proportional to their size N_p and number density d_p (see Table 3):

$$\sigma_p = \alpha_p M G b \sqrt{N_p d_p} \tag{17}$$

Thus, Equation (15) can be rewritten in the final form:

$$\Delta H(h) = \beta MGb\left(\sqrt{\alpha_d^2\rho_d + \alpha_p^2 N_p d_p + \frac{\alpha_l^2}{V_{pz}(h)}\int N_l(z)d_l(z)dV + \frac{\alpha_c^2}{V_{pz}(h)}\int N_c(z)d_c(z)dV} - \sqrt{\alpha_d^2\rho_d + \alpha_p^2 N_p d_p}\right) \quad (18)$$

Monnet [30] demonstrated that the obstacle strength of forest dislocations α_d and loops α_l are approximately 0.25 and 0.5, respectively. The obstacle strengths of particles (carbides) α_p and clusters α_c, treated by Monnet [30] on the basis of a combined consideration of prior work [56,57], depend on their number density and size:

$$\alpha_p = \left(\frac{ln(2\underline{D}/b)}{ln(l/b)}\right)^{3/2}\frac{ln(l/b)}{2\pi} \quad (19)$$

$$\alpha_c = \left(\frac{\Omega_{obs}}{\Omega_\infty}\frac{ln(2\underline{D}/b)}{ln(l/b)}\right)^{3/2}\frac{ln(l/b)}{2\pi} \quad (20)$$

where Ω_{obs} and Ω_∞ are shear resistance, suggested to be 2.4 GPa and 4.5 GPa, respectively [30]. l and $\underline{D}$ are the free distance between the obstacles (particles or clusters) and the harmonic average of l and d, respectively:

$$l = (Nd)^{-0.5} - d \quad (21)$$

$$\underline{D} = ld/(l+d) \quad (22)$$

For carbides, the characterized parameters were reported in previous work [32] and displayed in Table 3 in Section 3.1. The calculated obstacle strengths α_p are 0.89 and 0.91 for ANP-6 and ANP-10, respectively. For clusters, the value of α_c depends on depth because of the depth profile of the irradiation-induced clusters, but it is not significantly different along the depth. An averaged α_c along the depth for each condition was calculated, which is summarized in Table 7.

Table 7. Obstacle strength α_c for clusters.

Material	0.1 dpa	1 dpa
ANP-6	0.142	0.175
ANP-10	0.135	0.157

The results obtained for Case 2 are shown in Figure 9a,b for both materials.

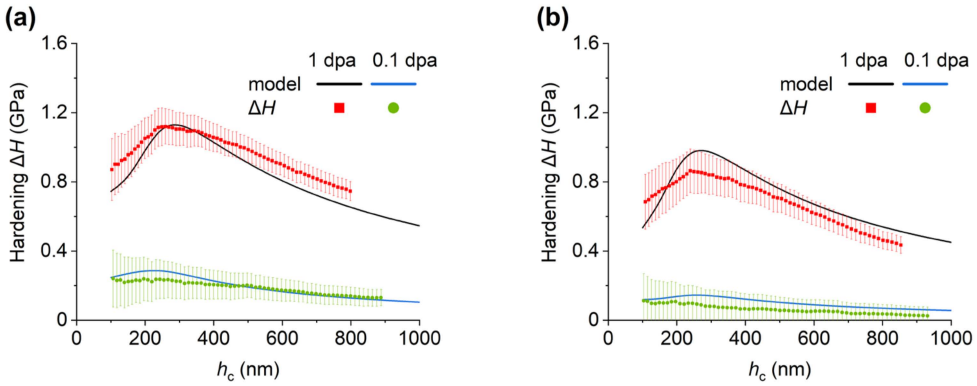

Figure 9. Case 2 model predictions with experiments for (**a**) ANP-6 and (**b**) ANP-10.

The predictions for Case 2 agree reasonably well with the experimental results in the whole range of contact depths for both materials and both irradiation conditions. This

is surprising because GNDs produced during the nanoindentation were not taken into account explicitly.

Returning to Case 1, it would be interesting to see how the obstacle strength introduced for Case 2 would modify the Case 1 prediction. This is straightforward because both obstacle strengths are larger for Case 2 than for Case 1, namely 0.5 instead of 0.333 for loops and the values given in Table 7 instead of 0.1 for clusters. As a consequence, Case 1, with the parameters adopted from Case 2, would give rise to an overestimation of the measured hardening for all conditions.

4.4. Case 3

In Case 3, the GNDs in the plastically deformed zone below the nanoindenter are taken into account. According to Nix and Gao [12], their density averaged over the plastic zone is inversely proportional to the contact depth:

$$\rho_{gnd}(h) = \frac{3\,tan^2\,\theta}{2b} \cdot \frac{1}{h} \tag{23}$$

However, several authors [47,48,58] have found a larger size of the plastic zone compared with the assumption made by Nix and Gao [12]. Taking the same total number of GNDs in the plastic zone, a larger plastic zone is equivalent to a smaller density of GNDs. In terms of the plastic zone size factor c introduced above, the factor of proportionality in Equation (23) has to be modified:

$$\rho_{gnd}(h) = \frac{3}{2\,tan\,\theta\,c^3 b} \cdot \frac{1}{h} \tag{24}$$

Still, the densities of GNDs based on Equations (23) and (24) depend inversely on contact depth (h). They are plotted in Figure 10.

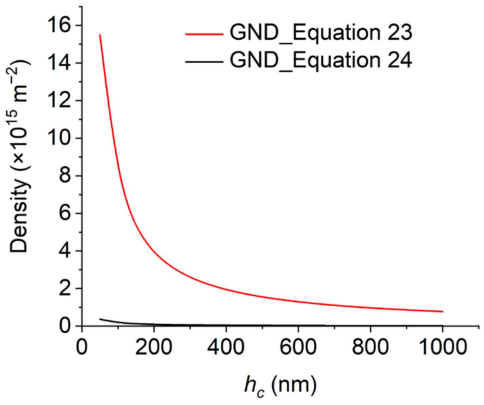

Figure 10. Density of GNDs according to Equations (23) and (24).

For a contact depth of 100 nm, the average densities of GNDs according to Equations (23) and (24) are 7.8 × 10^{15} m^{-2} and 1.8 × 10^{14} m^{-2}, respectively. Compared with Equation (18), hardening due to GNDs has to be taken into account to calculate the irradiation-induced hardness change:

$$\Delta H(h) = \beta MGb\left(\sqrt{\alpha_d^2\rho_{gnd}(h) + \alpha_d^2\rho_d + \alpha_p^2 N_p d_p + \frac{\alpha_l^2}{V_{pz}(h)}\int N_l(z)d_l(z)dV + \frac{\alpha_c^2}{V_{pz}(h)}\int N_c(z)d_c(z)dV} - \sqrt{\alpha_d^2\rho_{gnd}(h) + \alpha_d^2\rho_d + \alpha_p^2 N_p d_p}\right) \tag{25}$$

The density of GNDs is considered to be the same for the unirradiated and irradiated samples. Based on Case 2 (where GNDs are neglected), here referred to as GND_0, predictions with two different densities of GNDs have been applied. The prediction based on Equation (25) with Equations (23) and (24) are referred to as GND_1 and GND_2, re-

spectively. The Case 3 predictions and their comparisons with the experimental results are plotted in Figure 11.

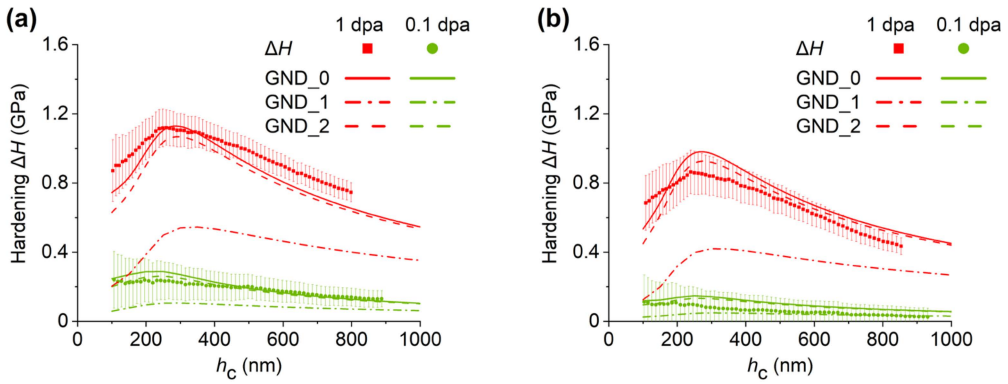

Figure 11. Case 3 model predictions with experiments for (**a**) ANP-6 and (**b**) ANP-10.

For GND_1, due to a much larger density of GNDs in the unirradiated and irradiated samples, the predicted irradiation hardening is considerably reduced compared with Case 2 (curve GND_0), which means the prediction underestimates the experimental results for all conditions. For GND_2 with a smaller density of GNDs, the reduction in the predicted irradiation hardening with respect to Case 2 is smaller than the experimental error.

4.5. Case 4

According to Mattucci et al. [31], the average density of GNDs for the irradiated condition is higher than for the unirradiated reference. This is because the radius of the plastic zone is smaller, while the number of GNDs is the same at equal contact depths. Introducing the subscript '*i*' for the irradiated condition, the following relation between the densities of GNDs holds:

$$\rho_{gnd,i}(h) = \left(\frac{c}{c_i}\right)^3 \rho_{gnd}(h) \tag{26}$$

Introducing Equation (26) into Equation (18) yields the Case 4 prediction of irradiation hardening, which is similar to Equation (25) but with a higher density of GNDs for the irradiated condition:

$$\Delta H(h) = \beta MGb\left(\sqrt{\alpha_d^2\left(\frac{c}{c_i}\right)^3\rho_{gnd}(h) + \alpha_d^2\rho_d + \alpha_p^2 N_p d_p + \frac{\alpha_l^2}{V_{pz}(h)}\int N_l(z)d_l(z)dV + \frac{\alpha_c^2}{V_{pz}(h)}\int N_c(z)d_c(z)dV} - \sqrt{\alpha_d^2\rho_{gnd}(h) + \alpha_d^2\rho_d + \alpha_p^2 N_p d_p}\right) \tag{27}$$

The relevant ratio of the size factors in Equation (26) can be estimated from the experimental data using Equations (9) and (10) based on the expanding cavity model. For this purpose, we need the yield stress of the unirradiated (see Table 6) and irradiated materials. In order to roughly estimate the yield stress of the ion-irradiated materials, we converted the difference of the measured indentation hardness at the peak position between the irradiated and unirradiated conditions into values of the irradiation-induced yield stress increase. The ratios of c/c_i used in Equation (27) are summarized in Table 8, along with the corresponding ratios of the densities of GNDs.

Table 8. Ratios of c/c_i and $\rho_{gnd,i}/\rho_{gnd}$ for both materials and irradiations.

	ANP-6, 0.1 dpa	ANP-6, 1 dpa	ANP-10, 0.1 dpa	ANP-10, 1 dpa
c/c_i	1.04	1.06	1.02	1.07
$\rho_{gnd,i}/\rho_{gnd}$	1.11	1.18	1.07	1.23

Based on the Case 2 prediction (denoted GND_0), Case 4 predictions with two different densities of GNDs for the unirradiated references, along with the densities of GNDs for the irradiated conditions according to Equation (26), have been applied. The prediction based on Equation (27) with Equations (23) and (24) are referred to as GND_3 and GND_4, respectively. The Case 4 predictions are shown in Figure 12 with the measured hardening.

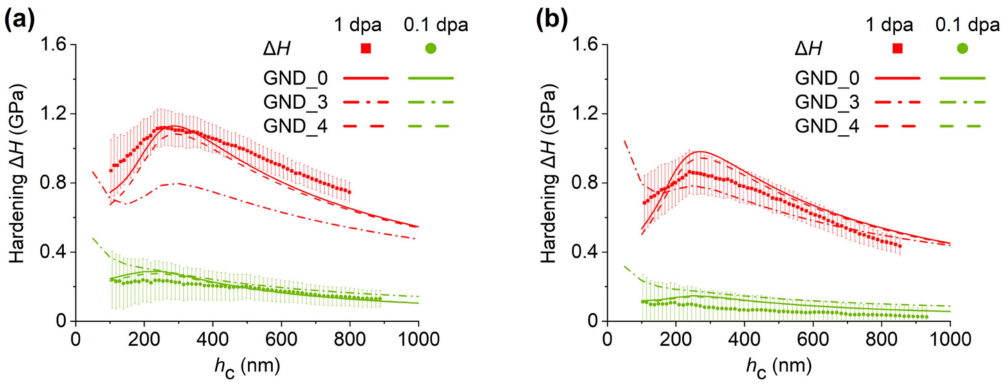

Figure 12. Case 4 model predictions with experiments for (**a**) ANP-6 and (**b**) ANP-10.

At large contact depths, ΔH is smaller for GND_3 than for GND_0 in the case of 1 dpa, but ΔH is larger for GND_3 than for GND_0 in the case of 0.1 dpa. For GND_3 at small contact depths, ΔH increases steeply at decreasing contact depth below 150 nm for both 0.1 dpa and 1 dpa and even exceeds GND_0 for 1 dpa. This is due to the large density of GNDs at small depths (Figure 10). For GND_4, there is a small reduction in ΔH compared with GND_0 in the entire range of contact depths and for both material and irradiation conditions. It is also interesting to note that GND_4 is very close to GND_2.

5. Discussion

5.1. Error Estimation

In the previous sections, errors in the model predictions were not considered. The following estimation is based on Equation (18), which is related to Case 2. As a rough and conservative estimate, only the errors of the prediction of ΔH at the peak position are calculated. Due to the structure of Equation (18), the errors arising from the unirradiated microstructure (forest dislocations and particles) are of minor importance. Moreover, the effect of the error of the pre-factor βMGb is obvious and is not emphasized in the discussion. The errors estimated for Case 2 are considered to be approximately representative of Cases 3 and 4 as well.

In essence, only the errors of the number density and mean size of the irradiation-induced loops and clusters are taken into account for the error estimation of the microstructure-informed prediction. As reported in Sections 3.2.1 and 3.2.2, for both loops and clusters, the error of number density and mean size are approximately 10% and 20%, respectively. Table 9 summarizes the estimated errors of the prediction of ΔH. The listed error estimates have to be taken into account for the following interpretation of the results plotted in Figures 9, 11 and 12. In particular, differences between two predictions that are smaller than the error are not reliable.

Table 9. Estimated error of the hardening predicted from the irradiated microstructure according to Equation (18).

Material/Irradiation	Estimated d(ΔH) (GPa)	d(ΔH)/ΔH
ANP-6, 0.1 dpa	0.070	24%
ANP-6, 1 dpa	0.241	21%
ANP-10, 0.1 dpa	0.066	45%
ANP-10, 1 dpa	0.247	25%

5.2. Discussion of Four Cases of Model Prediction

For the hardness of irradiated materials, a linear superposition of hardness contributions of the pre-existing and irradiated microstructures was applied in Case 1. Taking into account the errors, we have observed reasonable agreement for the 1 dpa irradiation and overestimations for the 0.1 dpa irradiation of both materials. Changes in the model parameters that would result in agreement for 0.1 dpa would give rise to underestimations for 1 dpa, in particular for ANP-6. Moreover, the adoption of the obstacle strengths from Case 2 would result in overestimations for all conditions. Thus, the prediction appears to be wrong or limited to specific conditions at best. Some authors also reported good agreement of predictions based on linear superposition with experimental results obtained from nanoindentation [17,51]. While this may be true for special materials or irradiation conditions, linear superposition is not a general law. In this context, combinations of linear and square superposition were proposed [28–30]. The present work indicates that two different values of displacement damage are useful to test the validity of different superposition rules.

Case 2, which is based on mixed superposition of the pre-existing and irradiated microstructures to calculate the hardness of irradiated material and on optimized expressions for the hardening contributions [30], shows a better prediction of the irradiation hardening than Case 1. In particular, Case 2 simultaneously predicts the measured irradiation-induced hardening well for the 0.1 and 1 dpa irradiations and for both materials. In this respect, it is important to note that we used the same model parameters as those reported by Monnet except for the conversion factor β, which does not appear in [30]. This means that the good agreement between prediction and experiment is not the result of a fitting procedure. It is interesting to note that the optimized values of the obstacle strength of loops and clusters are larger than the values used in Case 1. The use of the optimized values for Case 1 would result in worse predictions. At first glance, the good agreement in Case 2 is surprising because the role of GNDs is not considered. The discussion of Cases 3 and 4 below will shed a light on this.

Case 3 is based on Case 2 but adds the hardening contribution of GNDs assumed to exhibit the same density for the irradiated material and the unirradiated reference. The density of GNDs of the unirradiated reference depends on the assumption about the size of the plastic zone. The small size factor originally assumed by Nix and Gao [12] gives rise to a large average density of GNDs, which results in a strong underestimation of the measured irradiation hardening, as shown in Figure 11. A similar strong underestimation was also reported by Vogel et al. [17] using the same size factor. In the present study, we have additionally used a modified size factor, the modification arising from a match of the peak positions of predicted and measured hardening. The corrected size factor leads to a smaller density of GNDs and gives rise to a minor reduction in the predicted hardening, which is still close to the experimental hardening, according to Figure 11. This result indicates that the average density of GNDs was overestimated by the original Nix–Gao model. Indeed, the modified size factor results in good agreement between prediction and measurement.

Case 4 is also based on Case 2 but adds the hardening contribution of GNDs assumed to exhibit a higher density for the irradiated material than for the unirradiated reference, the excess density arising from the smaller plastic zone of the irradiated material according to the expanding cavity model. For a high average density of GNDs of the unirradiated reference, the prediction is piecewise larger and piecewise smaller than in Case 2, resulting in worse fits of the measured hardening, according to Figure 12. For a low density of GNDs, the prediction of irradiation hardening is similar to Cases 2 and 3, which means a good agreement with the measurement. Different densities of GNDs for irradiated and unirradiated materials were already introduced before by Mattucci et al. [31]. This assumption was motivated by the observation of a gap between the microstructure-informed prediction and the measurement of hardening in proton-irradiated Ni, especially for small contact depths h_c. In the present study, the comparison of GND_3 with GND_4 generally confirms the effect of the density of GNDs on the predicted hardness increase. However, in

contrast to [31], our microstructure-informed prediction without consideration of GNDs already agreed well with the measured hardening. We can conclude that, in the present case, the irradiation hardening mainly arises from the irradiation-induced defects, and the contribution of the higher density of GNDs in the irradiated material is of minor relevance. This situation can change at smaller contact depths than those considered in our study ($h_c < 100$ nm).

Summarizing the discussion of Cases 1 to 4, it is found that:

- The applicability of linear superposition of the hardening contributions arising from the pre-existing and irradiated microstructures is, at best, limited to specific conditions.
- Mixed (linear and square) superposition of the pre-existing and irradiated microstructures simultaneously predicts all the conditions covered by the present study well. Specifically, solid solution strengthening and grain boundary strengthening belong to linear superposition, which is dropped out for the hardening. Pre-existing forest dislocations, precipitates, irradiation-induced loops, and clusters are considered quadratically for the hardening contribution.
- The latter is even true without additional consideration of GNDs. However, a small to medium density of GNDs well below 10^{15} m^{-2} has a minor effect on the prediction and still results in good agreement with the measurements.
- In contrast, the additional consideration of a large density of GNDs gives rise to worse predictions of hardening. This indicates an upper bound for the real density of GNDs, the upper bound lying between Equations (23) and (24).
- A larger density of GNDs for an irradiated material compared with the unirradiated reference predicts an indirect increase in ΔH due to the smaller plastic zone size during nanoindentation in addition to the direct increase due to the irradiation-induced defects. Under the present conditions and in the covered range of contact depths h_c, the latter contribution is dominant.

5.3. Individual Hardness Contributions

The individual hardness contributions of the initial and irradiated microstructures in the present study are plotted as bar charts in Figure 13 for ANP-6 and Figure 14 for ANP-10. Additionally, the contribution of GNDs (plotted as lines) is added for comparison. The resulting plots do not represent the real total hardness of both materials, which depends on the kind of superposition of individual contributions. However, they provide a rough visualization of the percentage of different kinds of hardness contributions as a function of the contact depth.

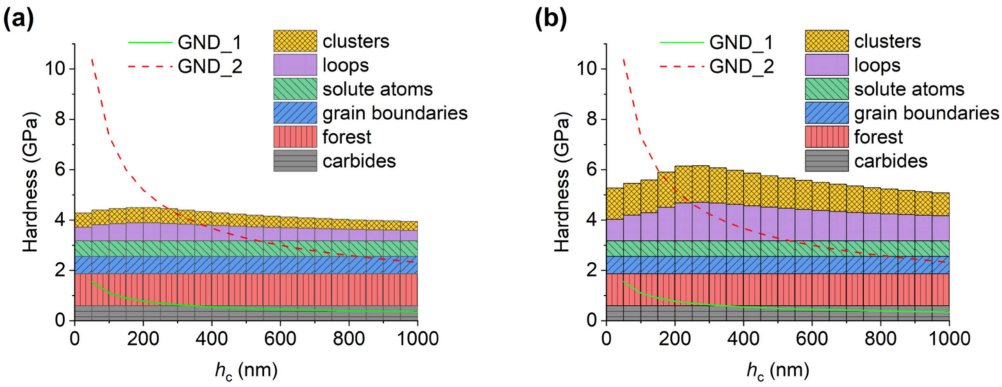

Figure 13. Hardness calculated for individual initial and irradiation-induced contributions in ANP-6 using microstructure data introduced in Section 3, (**a**) 0.1 dpa and (**b**) 1 dpa. The contribution of GNDs is shown for comparison.

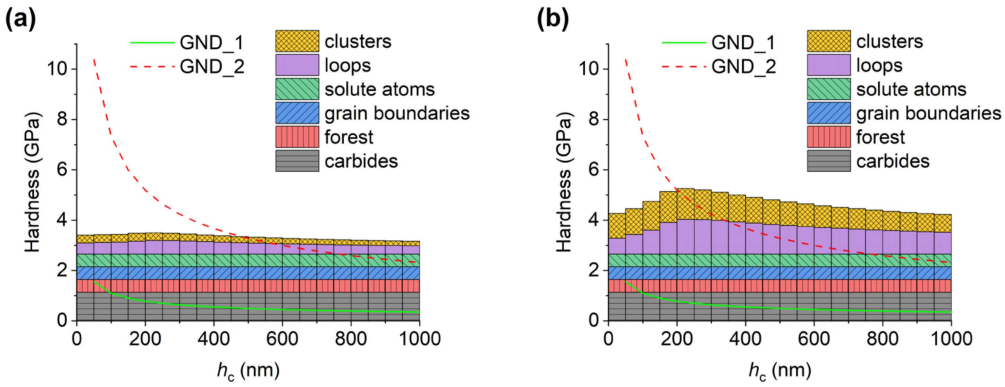

Figure 14. Hardness calculated for individual initial and irradiation-induced contributions in ANP-10 using microstructure data introduced in Section 3, (**a**) 0.1 dpa and (**b**) 1 dpa. The contribution of GNDs is shown for comparison.

The pre-existing (unirradiated) microstructure includes forest dislocations, particles (carbides), grain boundaries [32], and solute atoms calculated based on [59]. The pre-existing microstructure does not depend on depth, while the irradiated microstructure, including loops and clusters, is depth-dependent. For the irradiation-induced hardness, it is interesting to note that the contributions of loops and clusters are approximately equal for both materials and irradiations. Regarding the pre-existing microstructure, forest dislocations are dominant microstructure features in ANP-6, while the hardening of ANP-10 is affected mainly by carbides. The hardness contribution of GNDs produced by nanoindentation is similar for both materials and irradiations. Two different assumptions of the size of the plastic zone result in significantly different densities of GNDs and, thus, in different hardness contributions. For GND_1, which assumes a smaller size of the plastic zone, the hardness contribution of GNDs is dominant among all other contributions, especially at a small contact depth. However, as Figure 11 indicates, the prediction based on GND_1 does not fit the measurements well. The reason is the unrealistically small size of the plastic zone. Indeed, the GND_2 prediction based on a larger plastic zone size gives rise to better fits with the measurements (Figure 11) and to more realistic contributions of GNDs (Figures 13 and 14).

It is important to note that, according to Equation (23), the density of GNDs increases to very large values if the contact depth approaches zero. This is physically impossible, as pointed out by several authors [9,31,60,61]. The maximum possible density of GNDs was reported to be of the order of 10^{16} m^{-2} [60]. Such high densities of GNDs are not reached in the present study, which focused on the range of contact depths larger than 100 nm. Therefore, the effect of the maximum possible density of GNDs is not considered here.

6. Conclusions

In the present study, two different RPV steels, which were ion-irradiated up to the levels of displacement damage of 0.1 and 1 dpa, were investigated. For each condition (kind of steel and displacement damage level), nanoindentation was applied to measure the hardness as a function of the contact depth, taking into account a pile-up correction based on the elastic modulus. The initial and irradiated microstructures were characterized by different electron microscopy techniques and atom probe tomography. The estimated characteristics of the microstructure were taken as input for the prediction of hardening, which is also referred to as microstructure-informed hardness modeling. Four versions of the prediction were introduced. The main conclusions are:

- Linear superposition of the hardening caused by the microstructure features present in the pre-existing microstructures with the irradiation-induced hardening is, at best, limited to special conditions.

- Mixed superposition of the hardening contribution from the pre-existing and irradiated microstructures, along with reported values of the obstacle strength, predicts the hardening well for all conditions covered in the present study. The term "mixed" means "linear" for grain boundary hardening and solid solution hardening but "quadratic" for the other contributions considered.
- The irradiation-induced hardening from dislocation loops and solute atom clusters is similar, although the number density of loops is lower. This is because of the larger loop size and, more prominently, because of a higher obstacle strength.
- Based on the mixed superposition law, additional consideration of GNDs yields similar predictions, which also means a good agreement if the average density of GNDs is below 10^{15} m^{-2}. The agreement is worse if the average density of GNDs is above 10^{15} m^{-2}.

In a former work by Mattucci et al. on proton-irradiated Ni [31], a significant contribution to the measured irradiation-induced hardness increase was found to arise from the larger density of GNDs in the irradiated condition compared with the unirradiated reference. In the present study, the irradiation-induced hardness increase is governed by the irradiation-induced nanofeatures with a minor contribution arising from GNDs, no matter if their densities for the irradiated and unirradiated conditions are equal or slightly different.

Author Contributions: Conceptualization, L.L., F.B. and P.C.; methodology, L.L., F.B., J.-E.B., P.C., B.R., F.C., A.E. and A.D.; software, P.C. and L.L.; validation, L.L., F.B., P.C. and J.-E.B.; formal analysis, L.L., F.B., P.C., J.-E.B., B.R., F.C., A.E. and A.D.; investigation, L.L., J.-E.B., P.C., F.B., B.R., F.C., A.E. and A.D.; writing—original draft preparation, L.L. and F.B.; writing—review and editing, L.L., F.B., J.-E.B., P.C., D.R., B.R., F.C., A.E. and A.D.; supervision, P.C., F.B., D.R. and B.R.; project administration, F.B. and P.C.; funding acquisition, F.B. All authors have read and agreed to the published version of the manuscript.

Funding: This research was funded by project ENTENTE, Euratom research and training program 2019/2020 under grant agreement No. 900018.

Data Availability Statement: The raw data supporting the conclusions of this article will be made available by the authors on request.

Acknowledgments: The Ion Beam Center at Helmholtz-Zentrum Dresden-Rossendorf e. V., a member of the Helmholtz Association, is acknowledged for carrying out the ion irradiations. We would like to thank Shavkat Akhmadaliev for assistance. The use of the Ion Beam Center facilities and the support of its staff is gratefully acknowledged. APT analyses were performed on GENESIS platform instruments supported by the Région Haute-Normandie, the Métropole Rouen Normandie, CNRS via LABEX EMC3, and the French National Research Agency via "Investissements d'avenir" program (ANR-11-EQPX-0020).

Conflicts of Interest: The authors declare no conflict of interest.

References

1. Was, G.S.; Zinkle, S.J. *Toward the Use of Ion Irradiation to Predict Reactor Irradiation Effects*, 2nd ed.; Rudy, J.M., Konings, R.E.S., Eds.; Elsevier: Amsterdam, The Netherlands, 2020; Volume 1.
2. Jiao, Z.; Michalicka, J.; Was, G. Self-ion emulation of high dose neutron irradiated microstructure in stainless steels. *J. Nucl. Mater.* **2018**, *501*, 312–318. [CrossRef]
3. Xu, S.; Yao, Z.; Jenkins, M. TEM characterisation of heavy-ion irradiation damage in FeCr alloys. *J. Nucl. Mater.* **2009**, *386*, 161–164. [CrossRef]
4. Taller, S.; VanCoevering, G.; Wirth, B.D.; Was, G.S. Predicting structural material degradation in advanced nuclear reactors with ion irradiation. *Sci. Rep.* **2021**, *11*, 2949. [CrossRef] [PubMed]
5. Was, G.; Jiao, Z.; Getto, E.; Sun, K.; Monterrosa, A.; Maloy, S.; Anderoglu, O.; Sencer, B.; Hackett, M. Emulation of reactor irradiation damage using ion beams. *Scr. Mater.* **2014**, *88*, 33–36. [CrossRef]
6. Bai, X.; Han, Y.; Liaw, P.K.; Wei, L. Effect of Ion Irradiation on Surface Microstructure and Nano-Hardness of SA508-IV Reactor Pressure Vessel Steel. *J. Mater. Eng. Perform.* **2022**, *31*, 1981–1990. [CrossRef]

7. Iwata, K.; Takamizawa, H.; Ha, Y.; Shimodaira, M.; Okamoto, Y.; Honda, M.; Katsuyama, J.; Nishiyama, Y. EXAFS studies for atomic structural change induced by ion irradiation of a reactor pressure vessel steel. *Nucl. Instrum. Methods Phys. Res. Sect. B Beam Interact. Mater. At.* **2022**, *511*, 143–152. [CrossRef]
8. Gasparrini, C.; Xu, A.; Short, K.; Wei, T.; Davis, J.; Palmer, T.; Bhattacharyya, D.; Edwards, L.; Wenman, M. Micromechanical testing of unirradiated and helium ion irradiated SA508 reactor pressure vessel steels: Nanoindentation vs in-situ microtensile testing. *Mater. Sci. Eng. A* **2020**, *796*, 139942. [CrossRef]
9. Haušild, P. On the breakdown of the Nix-Gao model for indentation size effect. *Philos. Mag.* **2021**, *101*, 420–434. [CrossRef]
10. Hosemann, P.; Kiener, D.; Wang, Y.; Maloy, S.A. Issues to consider using nano indentation on shallow ion beam irradiated materials. *J. Nucl. Mater.* **2012**, *425*, 136–139. [CrossRef]
11. Ruiz-Moreno, A.; Hähner, P.; Kurpaska, L.; Jagielski, J.; Spätig, P.; Trebala, M.; Hannula, S.-P.; Merino, S.; de Diego, G.; Namburi, H. Round robin into best practices for the determination of indentation size effects. *Nanomaterials* **2020**, *10*, 130. [CrossRef]
12. Nix, W.D.; Gao, H. Indentation size effects in crystalline materials: A law for strain gradient plasticity. *J. Mech. Phys. Solids* **1998**, *46*, 411–425. [CrossRef]
13. Kasada, R.; Takayama, Y.; Yabuuchi, K.; Kimura, A. A new approach to evaluate irradiation hardening of ion-irradiated ferritic alloys by nano-indentation techniques. *Fusion Eng. Des.* **2011**, *86*, 2658–2661. [CrossRef]
14. Kasada, R.; Konishi, S.; Yabuuchi, K.; Nogami, S.; Ando, M.; Hamaguchi, D.; Tanigawa, H. Depth-dependent nanoindentation hardness of reduced-activation ferritic steels after MeV Fe-ion irradiation. *Fusion Eng. Des.* **2014**, *89*, 1637–1641. [CrossRef]
15. Kareer, A.; Prasitthipayong, A.; Krumwiede, D.; Collins, D.; Hosemann, P.; Roberts, S. An analytical method to extract irradiation hardening from nanoindentation hardness-depth curves. *J. Nucl. Mater.* **2018**, *498*, 274–281. [CrossRef]
16. Röder, F.; Heintze, C.; Pecko, S.; Akhmadaliev, S.; Bergner, F.; Ulbricht, A.; Altstadt, E. Nanoindentation of ion-irradiated reactor pressure vessel steels–model-based interpretation and comparison with neutron irradiation. *Philos. Mag.* **2018**, *98*, 911–933. [CrossRef]
17. Vogel, K.; Heintze, C.; Chekhonin, P.; Akhmadaliev, S.; Altstadt, E.; Bergner, F. Relationships between depth-resolved primary radiation damage, irradiation-induced nanostructure and nanoindentation response of ion-irradiated Fe-Cr and ODS Fe-Cr alloys. *Nucl. Mater. Energy* **2020**, *24*, 100759. [CrossRef]
18. Xiao, X.; Yu, L. Comparison of linear and square superposition hardening models for the surface nanoindentation of ion-irradiated materials. *J. Nucl. Mater.* **2018**, *503*, 110–115. [CrossRef]
19. Kapoor, G.; Chekhonin, P.; Kaden, C.; Vogel, K.; Bergner, F. Microstructure-informed prediction and measurement of nanoindentation hardness of an Fe-9Cr alloy irradiated with Fe-ions of 1 and 5 MeV energy. *Nucl. Mater. Energy* **2022**, *30*, 101105. [CrossRef]
20. Seeger, A.K. On the theory of radiation damage and radiation hardening. In Proceedings of the Second United Nations International Conference on The Peaceful Uses of Atomic Energy, Geneva, Switzerland, 1–13 September 1958; United Nations: New York, NY, USA, 1958; Volume 6, pp. 250–273.
21. Chen, D.; Murakami, K.; Dohi, K.; Nishida, K.; Soneda, N.; Li, Z.; Liu, L.; Sekimura, N. Depth distribution of Frank loop defects formed in ion-irradiated stainless steel and its dependence on Si addition. *Nucl. Instrum. Methods Phys. Res. Sect. B Beam Interact. Mater. At.* **2015**, *365*, 503–508. [CrossRef]
22. Shimodaira, M.; Toyama, T.; Yoshida, K.; Inoue, K.; Ebisawa, N.; Tomura, K.; Yoshiie, T.; Konstantinović, M.J.; Gérard, R.; Nagai, Y. Contribution of irradiation-induced defects to hardening of a low-copper reactor pressure vessel steel. *Acta Mater.* **2018**, *155*, 402–409. [CrossRef]
23. Fukumoto, K.-I.; Mabuchi, T.; Yabuuchi, K.; Fujii, K. Irradiation hardening of stainless steel model alloy after Fe-ion irradiation and post-irradiation annealing treatment. *J. Nucl. Mater.* **2021**, *557*, 153296. [CrossRef]
24. Fang, Q.; Peng, J.; Chen, Y.; Li, L.; Feng, H.; Li, J.; Jiang, C.; Liaw, P.K. Hardening behaviour in the irradiated high entropy alloy. *Mech. Mater.* **2021**, *155*, 103744. [CrossRef]
25. Chen, S.; Yuan, J.; Wang, S.; Mei, L.; Yan, J.; Li, L.; Zhang, Q.; Zhu, Z.; Lv, J.; Xue, Y. Towards a reliable nanohardness-dose correlation of ion-irradiated materials from nanoindentation tests: A case study in proton-irradiated vanadium. *Int. J. Plast.* **2023**, *171*, 103804. [CrossRef]
26. Lin, P.-d.; Nie, J.-f.; Lu, Y.-p.; Shi, C.-x.; Cui, S.-g.; Cui, W.-d.; He, L. Atomic irradiation defects induced hardening model in irradiated tungsten based on molecular dynamics and CPFEM. *Int. J. Plast.* **2024**, 103895. [CrossRef]
27. Yang, J.; Bai, J.; Li, J.; Fu, C.; Lei, Q.; Lin, J. Hardening behavior of nickel-base alloy irradiated by multi-energy Fe ions. *J. Mater. Res. Technol.* **2024**, *29*, 1000–1009. [CrossRef]
28. Foreman, A.; Makin, M. Dislocation movement through random arrays of obstacles. *Can. J. Phys.* **1967**, *45*, 511–517. [CrossRef]
29. Zhu, P.; Zhao, Y.; Lin, Y.-R.; Henry, J.; Zinkle, S.J. Defect-specific strength factors and superposition model for predicting strengthening of ion irradiated Fe18Cr alloy. *J. Nucl. Mater.* **2024**, *588*, 154823. [CrossRef]
30. Monnet, G. Multiscale modeling of irradiation hardening: Application to important nuclear materials. *J. Nucl. Mater.* **2018**, *508*, 609–627. [CrossRef]
31. Mattucci, M.; Cherubin, I.; Changizian, P.; Skippon, T.; Daymond, M. Indentation size effect, geometrically necessary dislocations and pile-up effects in hardness testing of irradiated nickel. *Acta Mater.* **2021**, *207*, 116702. [CrossRef]

32. Lai, L.; Chekhonin, P.; Akhmadaliev, S.; Brandenburg, J.-E.; Bergner, F. Microstructural Characterization of Reactor Pressure Vessel Steels. *Metals* **2023**, *13*, 1339. [CrossRef]
33. Hein, H. Deliverable of Euratom Project SOTERIA, D3.5—Set of Guidelines on Use of Experiments Carried Out in WP3, Grant Agreement No. 661913. 2019.
34. Ziegler, J.F.; Ziegler, M.D.; Biersack, J.P. SRIM–The stopping and range of ions in matter. *Nucl. Instrum. Methods Phys. Res. Sect. B Beam Interact. Mater. At.* **2010**, *268*, 1818–1823. [CrossRef]
35. Stoller, R.E.; Toloczko, M.B.; Was, G.S.; Certain, A.G.; Dwaraknath, S.; Garner, F.A. On the use of SRIM for computing radiation damage exposure. *Nucl. Instrum. Methods Phys. Res. Sect. B Beam Interact. Mater. At.* **2013**, *310*, 75–80. [CrossRef]
36. Kinchin, G.; Pease, R. The displacement of atoms in solids by radiation. *Rep. Prog. Phys.* **1955**, *18*, 1. [CrossRef]
37. Norgett, M.; Robinson, M.; Torrens, I.M. A proposed method of calculating displacement dose rates. *Nucl. Eng. Des.* **1975**, *33*, 50–54. [CrossRef]
38. Lefebvre, W.; Vurpillot, F.; Sauvage, X. *Atom Probe Tomography: Put Theory into Practice*, 1st ed.; Lefebvre, W., Vurpillot, F., Sauvage, X., Eds.; Academic Press: Cambridge, MA, USA, 2016.
39. Oliver, W.C.; Pharr, G.M. Measurement of hardness and elastic modulus by instrumented indentation: Advances in understanding and refinements to methodology. *J. Mater. Res.* **2004**, *19*, 3–20. [CrossRef]
40. Oliver, W.C.; Pharr, G.M. An improved technique for determining hardness and elastic modulus using load and displacement sensing indentation experiments. *J. Mater. Res.* **1992**, *7*, 1564–1583. [CrossRef]
41. *Standard DIN EN ISO 14577-1*; Metallic Materials-Instrumented Indentation Test for Hardness and Materials Parameters. 2015. Available online: www.beuth.de (accessed on 18 February 2024).
42. Hardie, C.D.; Roberts, S.G.; Bushby, A.J. Understanding the effects of ion irradiation using nanoindentation techniques. *J. Nucl. Mater.* **2015**, *462*, 391–401. [CrossRef]
43. Zhu, P.; Zhao, Y.; Agarwal, S.; Henry, J.; Zinkle, S.J. Toward accurate evaluation of bulk hardness from nanoindentation testing at low indent depths. *Mater. Des.* **2022**, *213*, 110317. [CrossRef]
44. Heintze, C.; Bergner, F.; Akhmadaliev, S.; Altstadt, E. Ion irradiation combined with nanoindentation as a screening test procedure for irradiation hardening. *J. Nucl. Mater.* **2016**, *472*, 196–205. [CrossRef]
45. Ghosh, G.; Olson, G. The isotropic shear modulus of multicomponent Fe-base solid solutions. *Acta Mater.* **2002**, *50*, 2655–2675. [CrossRef]
46. Stoller, R.; Zinkle, S. On the relationship between uniaxial yield strength and resolved shear stress in polycrystalline materials. *J. Nucl. Mater.* **2000**, *283*, 349–352. [CrossRef]
47. Dolph, C.K.; da Silva, D.J.; Swenson, M.J.; Wharry, J.P. Plastic zone size for nanoindentation of irradiated Fe–9% Cr ODS. *J. Nucl. Mater.* **2016**, *481*, 33–45. [CrossRef]
48. Johnson, K. The correlation of indentation experiments. *J. Mech. Phys. Solids* **1970**, *18*, 115–126. [CrossRef]
49. Gao, X.-L.; Jing, X.; Subhash, G. Two new expanding cavity models for indentation deformations of elastic strain-hardening materials. *Int. J. Solids Struct.* **2006**, *43*, 2193–2208. [CrossRef]
50. Hein, H.; Gundermann, A.; Gillemot, F.; Serrano, M.; Hernandez, M.; Al-Mazouzi, A.; Todeschini, P.; Bergner, F.; Brumovsky, M.; Kytka, M.; et al. Deliverable D3.1 of Euratom project LONGLIFE, Documentation and data of materials for microstructural analysis, Grant Agreement No. 249360. 2012.
51. Samuha, S.; Bickel, J.; Mukherjee, T.; DebRoy, T.; Lienert, T.; Maloy, S.; Lear, C.; Hosemann, P. Mechanical performance and microstructure of the grade 91 stainless steel produced via Directed Energy deposition laser technique. *Mater. Des.* **2023**, *227*, 111804. [CrossRef]
52. Wagner, A.; Ulbricht, A.; Bergner, F.; Altstadt, E. Influence of the copper impurity level on the irradiation response of reactor pressure vessel steels investigated by SANS. *Nucl. Instrum. Methods Phys. Res. Sect. B Beam Interact. Mater. At.* **2012**, *280*, 98–102. [CrossRef]
53. Queyreau, S.; Monnet, G.; Devincre, B. Orowan strengthening and forest hardening superposition examined by dislocation dynamics simulations. *Acta Mater.* **2010**, *58*, 5586–5595. [CrossRef]
54. Ebeling, R.; Ashby, M. Dispersion hardening of copper single crystals. *Philos. Mag.* **1966**, *13*, 805–834. [CrossRef]
55. Hirsch, P.B.; Humphreys, F. The deformation of single crystals of copper and copper-zinc alloys containing alumina particles-I. Macroscopic properties and workhardening theory. *Proc. R. Soc. Lond. A Math. Phys. Sci.* **1970**, *318*, 45–72. [CrossRef]
56. Bacon, D.; Kocks, U.; Scattergood, R. The effect of dislocation self-interaction on the Orowan stress. *Philos. Mag.* **1973**, *28*, 1241–1263. [CrossRef]
57. Friedel, J. *Dislocations: International Series of Monographs on Solid State Physics*; Addison-Wesley: Reading, MA, USA, 1964; Volume 3.
58. Durst, K.; Backes, B.; Göken, M. Indentation size effect in metallic materials: Correcting for the size of the plastic zone. *Scr. Mater.* **2005**, *52*, 1093–1097. [CrossRef]
59. Chauhan, A.; Bergner, F.; Etienne, A.; Aktaa, J.; De Carlan, Y.; Heintze, C.; Litvinov, D.; Hernandez-Mayoral, M.; Oñorbe, E.; Radiguet, B. Microstructure characterization and strengthening mechanisms of oxide dispersion strengthened (ODS) Fe-9% Cr and Fe-14% Cr extruded bars. *J. Nucl. Mater.* **2017**, *495*, 6–19. [CrossRef]

60. Huang, Y.; Zhang, F.; Hwang, K.; Nix, W.; Pharr, G.; Feng, G. A model of size effects in nano-indentation. *J. Mech. Phys. Solids* **2006**, *54*, 1668–1686. [CrossRef]
61. Ruiz-Moreno, A.; Hähner, P. Indentation size effects of ferritic/martensitic steels: A comparative experimental and modelling study. *Mater. Des.* **2018**, *145*, 168–180. [CrossRef]